Rational Construction of Strongly Coupled Metal−Metal Oxide−Graphene Nanostructure with Excellent Electrocatalytic Activity and Durability

Haoliang Huang,[†] Yingju Liu,*[,†,‡] Qiongzhi Gao,[†] Weishuo Ruan,[†] Xiaomin Lin,[†] and Xin Li[†]

[†]Institute of Biomaterials, Department of Applied Chemistry, College of Sciences, South China Agricultural University, Guangzhou 510642, China

[‡]State Key Laboratory of Chem/Biosensing & Chemometrics, Hunan University, Changsha 410082, China

Ⓢ *Supporting Information*

ABSTRACT: The interaction within heterogeneous nanostructures can provide a great opportunity to radically enhance their electrocatalytic properties and increase their activity and durability. Here a rational, simple, and integrated strategy is reported to construct uniform and strongly coupled metal−metal oxide−graphene nanostructure as an electrocatalyst with high performance. We first simply synthesized the interacted SnO_2−prGO (protected and reduced graphene oxide) hybrid with SnO_2 nanoparticles (∼4 nm) selectively anchored on the oxygenated defects of rGO using an in situ redox and hydrolysis reaction. After the deposition of Pt, uniform Pt NPs are found to contact intimately and exclusively with the SnO_2 phase in the SnO_2−prGO hybrid. This constructed nanostructure (Pt-SnO_2−prGO) exhibits significantly improved electrocatalytic activity (2.19-fold) and durability (2.08-fold) toward methanol oxidation over that of the state-of-the-art Pt/C catalyst. The detailed explanation of the strong coupling between SnO_2 and graphene as well as between Pt and SnO_2 is discussed, revealing that such a process can be used to immobilize various metal catalysts on metal-oxide-decorated catalysts for realizing advanced catalytic systems with enhanced performance.

KEYWORDS: *strong coupling, heterogeneous nanostructures, electrocatalyst, SnO_2, graphene, methanol oxidation reaction*
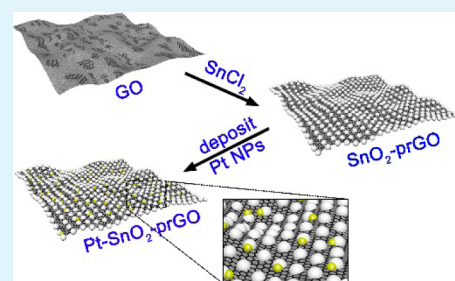
1. INTRODUCTION

Heterogeneous nanostructured material exhibits not only the intrinsic properties of constitutive components but also the synergy between support and the supported phase as well.[1−4] The most cited reasons are the so-called support interaction, tuning the electronic and chemical properties of the active phase to achieve better performance via chemical bonding and associated charge transfer at the interface.[5] Unfortunately, with respect to fuel cell technology, carbon materials, widely used as electrocatalyst supports, are categorized as a current collector with high surface area rather than a "real" support for platinum nanoparticles (Pt NPs) in the sense of the heterogeneous catalyst, because of its inherent lack of interaction with metal.[6,7] Often, it is found that metal−metal oxide nanostructures exhibit surprisingly high catalytic activity and durability, which has been attributed to "strong metal−support interaction" (SMSI)[5,7−9] or even "electronic metal−support interaction" (EMSI).[10] Additionally, strong chemical attachment and electrical coupling between metal oxide and nanocarbon (e.g., carbon nanotube, graphene) have been extensively reported.[11] As we know, metal oxide suffers from insufficient electrical conductivity and low surface area, which are the prerequisites for the support of the electrocatalyst.[6] In this context, combining metal oxide and nanocarbon might be a solution

to develop a proper heterogeneous nanostructured electrocatalyst.

Tin oxide (SnO_2) was selected as the metal oxide phase due to its features including cocatalytic functionality,[1] electronic interaction with Pt,[12] stability in a harsh environment,[13] and low price and environmental benignity. Graphene (or reduced graphene oxide, rGO) has inspired a flurry of interest due to its extraordinary properties such as high specific surface area, excellent conductivity, and relatively high anticorrosion.[11,14] Although great strides have been achieved toward the preparation of SnO_2−rGO nanocomposite for battery application,[15−17] the same progress has not been attained in fuel cells, because the electrocatalyst is typically surface- and interface-sensitive.[18] For the synthesis of cocatalytic as well as robust SnO_2−rGO for Pt support, four major obstacles need to be addressed: (i) the synthesis of high surface-exposed SnO_2 nanocrystals which are able to create strong linkage with Pt but difficult to be stabilized; (ii) selective and direct contact between SnO_2 and Pt; (iii) sufficient interaction between SnO_2 and rGO to improve the electrical conductivity of the hybrid; (iv) the restacking of rGO sheets and the corrosion on the

ACS Publications © 2014 American Chemical Society

10258

dx.doi.org/10.1021/am5016606 | ACS Appl. Mater. Interfaces 2014, 6, 10258−10264

oxygenated defect cluster (∼30% domain of rGO).[19] Unfortunately, to our knowledge, there are no studies to solve the above problems. In this work, by integrating the interfacial interaction of Pt-SnO_2 and SnO_2−graphene, the resulting strongly coupled Pt-SnO_2−rGO could possess the complementary advantages of tin oxide and graphene, thus enhancing the electrocatalytic performance of Pt NPs.

Herein, we rationally construct SnO_2−prGO (protected and reduced graphene oxide) nanostructured hybrids for the application of Pt NPs support. This approach is based on the in situ redox and hydrolysis reaction between $SnCl_2$ and GO, which conceptually makes the full advantages of metal oxide and graphene phase. As a result, the SnO_2−prGO hybrid exhibits an exciting and desirable nanostructure where ultrafine SnO_2 NPs are exclusively anchored on the defects of rGO and protected from corrosion, as well as surrounded by a conductive graphene-like network. Most notably, after the deposition of Pt on the SnO_2−prGO support, uniform Pt NPs are found to contact intimately and exclusively with SnO_2 NPs, which enable the cocatalytic effect from the SnO_2 phase. Relative to Pt-rGO and Pt/C, the strongly coupled Pt-SnO_2−prGO nanostructured hybrid electrocatalyst exhibits a significantly improved electrocatalytic activity and durability toward the methanol oxidation reaction (MOR). It is proposed that the improved performance is the result of the synergistic effect from the interactions between SnO_2 and graphene as well as between Pt and SnO_2.

2. EXPERIMENTAL SECTION

2.1. Chemicals. Graphite was purchased from Alfa Aesar, $SnCl_2 \cdot 2H_2O$ was purchased from Aladdin Industrial, Inc., and $H_2PtCl_6 \cdot 6H_2O$ was purchased from Shanghai July Chemical Co., Ltd. Unless otherwise stated, all the reagents were of analytical grade and used as received without further purification.

2.2. Synthesis of SnO_2−prGO. The graphite oxide was synthesized from natural graphite powder on the basis of the improved Hummers method.[20] After ultrasonication of the graphite oxide dispersion for 30 min, a homogeneous GO aqueous dispersion (3.05 mg/mL) was obtained. In a typical preparation of SnO_2−rGO, 3.28 mL of GO aqueous dispersion was diluted into 70 mL, and then 50 mg of $SnCl_2 \cdot 2H_2O$ was added. After 20 min of ultrasonication treatment, the mixture was heated at 70 °C for 3 h, and then it was transferred into a Teflon-lined autoclave with a stainless steel shell and heated at 120 °C for 12 h. The resultant black products were washed with water and ethanol for several times, isolated by centrifugation, and finally dried at 50 °C in an oven.

2.3. Loading of Pt on SnO_2−prGO. The Pt-SnO_2−prGO electrocatalyst was prepared using the modified formate process.[21,22] First, 20 mg of SnO_2−prGO hybrid was dispersed into 20 mL of ethylene glycol (EG) by ultrasonication. Then, a predetermined amount of H_2PtCl_6 aqueous solution was dropwise added. After vigorous stirring for 30 min, 100 mg of sodium formate was added. The mixture was heated at around 50 °C for 2 h under continuous magnetic stirring. After cooling to room temperature, the product was washed with ethanol and water for several times, isolated with centrifugation, and then dried at 50 °C in an oven. For comparison, hydrazine-reduced rGO sheets were loaded with Pt NPs using the same process, and Pt/C was synthesized through the conventional polyol method.[23] The Pt loading of the as-prepared catalyst was controlled as 20 wt %.

2.4. Material Characterization. Powder X-ray diffraction (XRD) measurement was performed using the Rigaku D/Max-2200 vpc with Cu Kα radiation. The product morphology and microstructure were studied by transmission electron microscopy (TEM; FEI, Tecnai 12, 100 kV) and high-resolution transmission electron microscopy (HRTEM; JEOL, JEM-2100HR, 200 kV). The high-angle annular dark field-scanning transmission electron microscope (HAADF-STEM) images and element analysis mapping were obtained with Tecnai G^2 F20 S-TWIN HRTEM. The surface properties of the samples were analyzed with X-ray photoelectron spectroscopy (XPS, Thermo-VG Scientific, ESCALAB 250) using an Al Kα X-ray source. The zeta potentials were measured on a Zetasizer Nano ZS (Malvern Instruments, Southborough, U.K.).

2.5. Electrochemical Measurements. The electrochemical measurements were carried out with a standard three-electrode system on an IM6ex electrochemical workstation (Zahner, Germany) using a platinum foil and a saturated calomel electrode (SCE) as the counter and reference electrode, respectively. For convenience, all the electrode potentials are referenced to a reversible hydrogen electrode (RHE). To prepare the catalyst suspension, 5 mg of catalysts were first dispersed in a 2.5 mL aqueous solution containing 1.25 mL of isopropanol and 50 μL of 5 wt % Nafion solution via ultrasonication for 15 min. Then, an aliquot of catalyst suspension was pipetted onto the prepolished glassy carbon electrode, leading to a Pt loading of about 31.83 μg cm^{-2} for all catalysts. The catalyst films were dried overnight before electrochemical measurements.

In order to get rid of any effect due to the Nafion film, the working electrodes were treated by continuous cyclic voltammetry (CV) between 0.05 to 1.2 V at a scan rate of 50 mV s^{-1} until a steady CV was obtained in N_2-saturated 0.5 M H_2SO_4 solution. Electrochemically active surface area (ECSA) was calculated by integrating the hydrogen absorption charges in the last cycle. The methanol oxidation experiments were conducted in a 2 M CH_3OH + 0.1 M H_2SO_4 electrolyte at a scan rate of 50 mV s^{-1}. Chronoamperometry (CA) curves were recorded at 0.80 V in a solution of 2 M CH_3OH + 0.1 M H_2SO_4 for 4 h to investigate the long-term performance of the as-prepared electrocatalysts. For CO stripping voltammetry, CO gas was purged into N_2-saturated 0.5 M H_2SO_4 at a position close to the working electrode for 20 min. After the excess CO was purged out with N_2 for 20 min, the CO stripping voltammetry was performed at a scan rate of 10 mV s^{-1}.

3. RESULTS AND DISCUSSION

3.1. Morphology and Structural Characterization. Figure 1 shows the XRD patterns of GO, SnO_2−prGO and Pt-SnO_2−prGO. GO has a sharp diffraction peak at 10°, corresponding to a (002) interplanar spacing of 0.88 nm. However, for the resultant SnO_2−prGO hybrid, the diffraction peak of layered GO disappeared, which might be attributed to the reduction of GO.[15] In addition, no apparent diffraction peak of graphene can be observed, implying that SnO_2 nanocrystals were efficiently deposited on the graphene surface and prevented the restacking of graphene sheets. Moreover, all peaks in the pattern of this hybrid can be unambiguously indexed to tetragonal rutile SnO_2 structure (JCPDS card no. 40-1445). The average crystallite from broad XRD peaks corresponded to about 4.3 nm, suggesting the ultrafine size of SnO_2. For the as-synthesized Pt-SnO_2−prGO, the SnO_2 phase
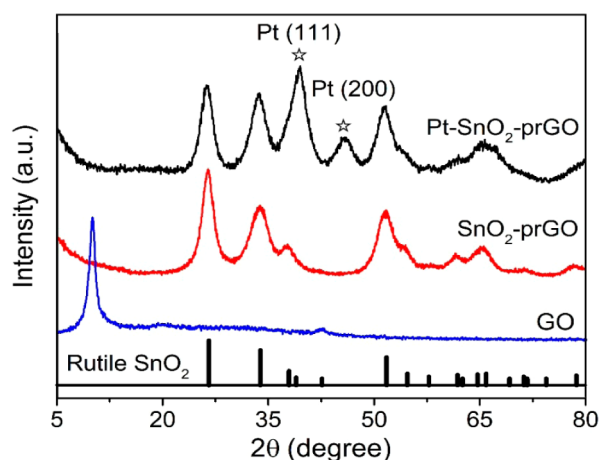
Figure 1. XRD pattern of GO, SnO_2–prGO, and Pt-SnO_2–prGO.

still remains the original rutile structure, meanwhile, two additional peaks that located at about 39.8° and 46.2° can be indexed to the face centered cubic (fcc) structure of pure Pt.

X-ray photoelectron spectroscopy (XPS) was performed to investigate the surface composition and chemical states of the species in as-synthesized samples. Figure 2a shows the survey
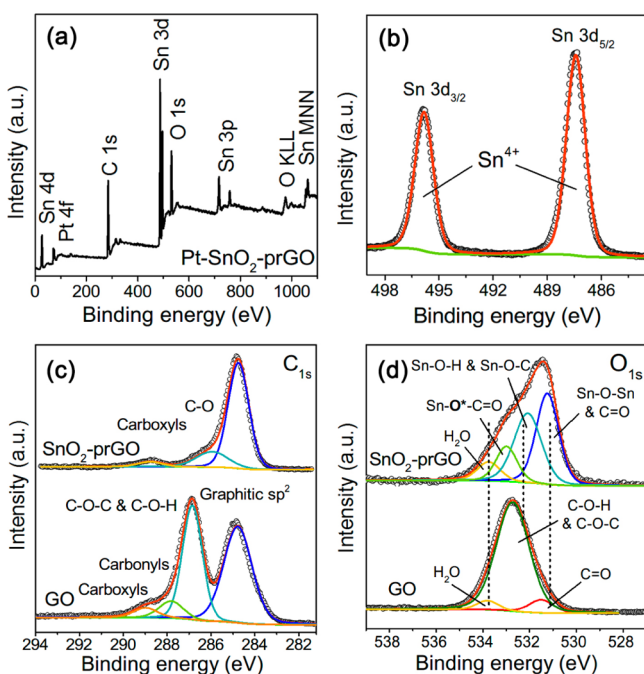

Figure 2. Survey XPS spectrum of Pt-SnO_2–prGO (a). Sn 3d spectrum of SnO_2–prGO (b). C 1s spectra of GO and SnO_2–prGO (c). O 1s spectra of GO and SnO_2–prGO (d).

spectrum of Pt-SnO_2–prGO, where four elements including C, O, Sn, and Pt were detected. In the formation of the SnO_2–prGO hybrid, both the oxidation of Sn^{2+} and the reduction of GO should be involved: (1) the existence of SnO_2 was confirmed by Sn 3d spectrum in Figure 2b where two symmetrical peaks at 495.8 and 487.4 eV are ascribed to Sn^{4+};[16,24] (2) the reduction of GO is confirmed by significantly improving the intensity of sp^2-hybridized C−C bonds at 284.8 eV, decreasing the oxygen-containing carbon including hydroxyl and epoxide C−O group at 286.8 eV, carbonyl C=

O group at 287.8 eV, and carboxyl O−C=O group at 289.0 eV,[25] as analyzed from the deconvoluted C 1s spectra of as-prepared GO and SnO_2−prGO hybrid in Figure 2c. However, a small amount of oxygenated groups (O−C=O and C−O) still remain in rGO, which can be also found in SnO_2/rGO composites, even though the amount of Sn^{2+} is excessive. Such remaining oxygenated species probably afford the interfacial interaction between SnO_2 NPs and rGO sheets, which can be further corroborated by comparing the deconvoluted O 1s spectra of SnO_2−rGO with that of GO (Figure 2d). The peak at the binding energy of 531.2 eV corresponds to the lattice oxygen of SnO_2 (Sn−O−Sn)[26] and C=O groups, whereas the peak at 533.8 eV is assigned to molecular water.[27] Interestingly, the additional two peaks of SnO_2−prGO cannot be assigned to the C−OH and/or C−O−C peak centered at 532.6 eV of GO, which indicates that the change of chemical environment for certain oxygenated species occur after the deposition of SnO_2 NPs. The chemical shift of the O 1s spectrum is related to electronegativity of bonded atoms. Because the Sn−O−Sn specie has lower O 1s binding energy than that of C−O−C species, the peak at 532.1 and 533.0 eV might be assigned to the bond between SnO_2 and the remaining oxygenated groups, that is, Sn−O−C and Sn−O*−C=O, respectively. Additionally, considering the small size of SnO_2 NPs in SnO_2−prGO, the peak at 532.1 eV should be ascribed to Sn−O−H species on the surface of SnO_2 NPs as well.[26] As a result, we believe that the oxygen bridge is the contributor for the linkage between SnO_2 NPs and rGO. More interestingly, the SnO_2−prGO exhibit a novel and exciting structure; that is, all oxygenated defects of rGO are bonded with SnO_2 NPs, whereas the graphene-like domain are exposed.

The morphology of SnO_2−prGO and Pt-SnO_2−prGO samples was further elucidated by TEM. Figure 3a shows that the SnO_2−prGO have sheet-like morphology with some corrugations, whereas a large number of ultrafine SnO_2 NPs are homogeneously dispersed on the rGO sheets. Several darker nanoparticles can be observed in the magnified TEM image (Figure S1), suggesting the overlap of SnO_2 NPs which are anchored on both sides of rGO sheets. The HRTEM image of SnO_2−prGO could provide more information about structure such as particle size and crystal lattice. Two well-defined lattice spacings of ∼0.26 and ∼0.33 nm correspond to the (101) planes and (110) planes of rutile SnO_2, respectively (Figure 3d). The particle size of SnO_2 is about 4 nm, which is in agreement with the XRD result. It is generally acknowledged that smaller particles have a higher tendency to aggregate and decrease the surface area, especially in nanoscale. However, both ultrafine and uniformly dispersed SnO_2 NPs are obtained in the present system. Combined with the XPS result, this specific phenomenon can be ascribed to the interfacial interaction between SnO_2 and rGO, which is strong enough to stabilize ultrafine SnO_2 NPs.

To investigate the distribution of Pt NPs on SnO_2−prGO, the atomic-number-sensitive HAADF-STEM and elemental mapping of Sn, O, and Pt were used. Figure S2 and Figure 3b show the bright-field TEM image and HAADF-STEM image of Pt-SnO_2−prGO, respectively. There is no obvious distinction in bright-field TEM image before and after the deposition of Pt on SnO_2−prGO. But the atomic-number-sensitive HAADF-STEM image reveals that Pt NPs are also highly dispersed on the SnO_2−prGO hybrid, which is also confirmed by the elemental mapping of Sn, O, and Pt (Figure 3c) on the selected area of HAADF-STEM. In contrast, the Pt NPs directly on rGO sheets
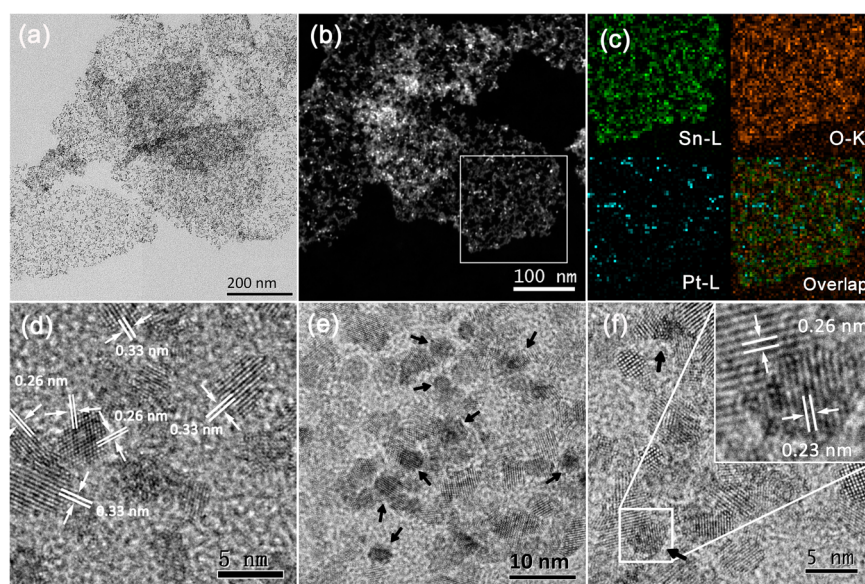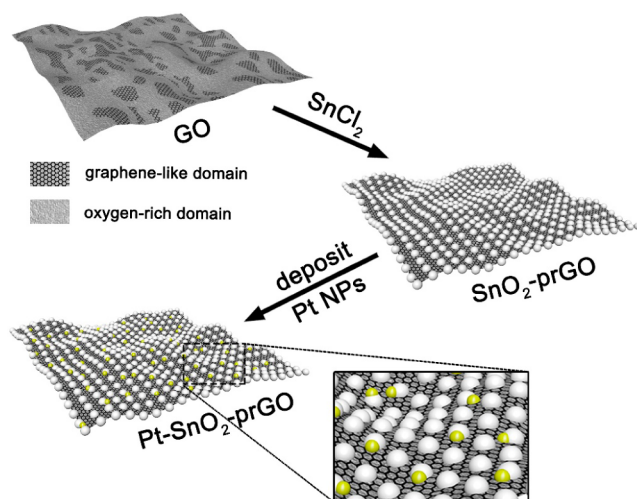
Figure 3. TEM images of SnO_2−prGO (a). HAADF-STEM image of Pt-SnO_2−prGO (b). Elemental mapping for Sn, O, Pt, and the overlap of these three elements (c). HRTEM images of SnO_2−prGO (d) and Pt-SnO_2−prGO (e, f) (the Pt NPs are marked by black arrow).

display a certain degree of aggregation (Figure S3), suggesting that ultrafine SnO_2 NPs can improve the dispersion of Pt NPs. To gain further insight into the detailed nanostructure, we distinguished between Pt NPs and SnO_2 NPs through carefully measuring the lattice fringe of all nanoparticles in high-resolution TEM of Pt-SnO_2−prGO, as shown in Figure 3e,f. Remarkably, it can be also seen that Pt NPs with about 3 nm in diameter are selectively attached to SnO_2 NPs. The inset image of Figure 1d further shows that crystalline Pt NPs (0.23 nm corresponding to the (111) planes of fcc Pt) are directly attached at the grain boundaries of the SnO_2 NPs, indicating that Pt NPs interact strongly with the surfaces of the SnO_2 NPs.

3.2. Possible Mechanism for the Formation of SnO_2−prGO and Pt-SnO_2−prGO. The possible mechanism for the formation of SnO_2−prGO and Pt-SnO_2−prGO is schematically depicted in Scheme 1. First, GO sheets, a precursor of graphene, have been recognized as anionic surfactant which possesses both hydrophilic (oxygen-rich domain) and hydro-

phobic (carbon-rich graphene-like domain) segments.[28,29] Therefore, when mixed with GO aqueous solution, Sn^{2+} cations are attracted on negative charged oxygen-rich domains of GO via electrostatic attraction, which are confirmed by the reversed zeta potential (after adding $SnCl_2$, the zeta potential is found to be shifted from −65.2 to 46.2 mV). Moreover, Sn^{2+} is an effective $(E^0(Sn^{4+}/Sn^{2+}) = 0.151$ V) and efficient (two-electron transfer process) reducing agent. In this contribution, the strongly coupled SnO_2−prGO hybrid, where ultrafine SnO_2 NPs are not only exclusively anchored on the defects of rGO and protected them from corrosion but also surrounded by the conductive graphene-like network as well, can be successfully synthesized via the in situ redox and hydrolysis reaction between GO and $SnCl_2$. In order to suppress the hydrolysis of Sn^{2+} in solution and ensure the predominance of the in situ reaction between the reactants, the mixture of $SnCl_2$ and GO aqueous solution must be stirred first at relatively high temperature. Otherwise, the phase separation of SnO_2 (white color) and SnO_2−prGO (black color) was visible to the naked eye (Figure S4).

Second, the selective deposition of Pt NPs on the surface of SnO_2 can be explained on the basis of the unique structure of SnO_2−prGO. The oxygenated groups of the graphene phase which serve as the nucleation site for Pt have already bonded covalently with SnO_2 NPs, although for the SnO_2 phase, the hydroxyls (OH) terminated on the surface of ultrafine SnO_2 NPs are exposed. It has been substantially reported that OH groups of metal oxides are capable of stabilizing noble metal nanoparticles.[9,30,31] To further probe the interaction between Pt and SnO_2, the binding energy of Pt 4f in Pt-SnO_2−prGO, Pt-rGO, and Pt/C were detected by XPS. Figure S5 shows the Pt 4f spectra, where the Pt-rGO and Pt/C electrocatalyst exhibits two similar peaks at 71.5 and 74.9 eV. However, these Pt 4f peaks shifted to lower binding energies (about 0.5 eV) as for the Pt-SnO_2−prGO, indicating the strong metal support interaction (SMSI) between Pt and SnO_2.[32,33]

In light of the above characterization and discussion, we believe that the complementary and interacted SnO_2−prGO hybrid have been successfully synthesized via an in situ and

Scheme 1. Schematic Illustration of the Preparation of the Pt-SnO_2−prGO Electrocatalyst

synergetic strategy. We expect that the resulting Pt-SnO$_2$−prGO nanostructured hybrid electrocatalysts with strong coupling could fully utilize the metal oxide and graphene phase to improve the activity and durability.

3.3. Electrochemical Performance of Pt-SnO$_2$−rGO.

The electrocatalytic properties of the Pt-SnO$_2$−prGO nanostructured hybrid toward methanol electro-oxidation were benchmarked against both Pt-rGO and Pt/C. Figure 4a
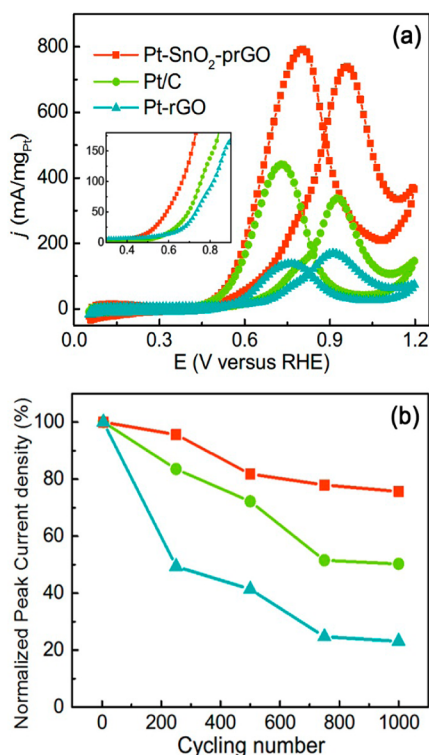

Figure 4. CV curves (a) and loss of forward peak current density with the number of CV cycles (b) on Pt-SnO$_2$−prGO, Pt/C, and Pt-rGO in 2 M CH$_3$OH + 0.1 M H$_2$SO$_4$ solution with a sweep rate of 50 mV s^{-1}.

shows the cyclic voltammograms (CVs) in 0.1 M H$_2$SO$_4$ and 2.0 M CH$_3$OH solution at a scan rate of 50 mV s^{-1}. The forward peak current density of the Pt-SnO$_2$−prGO electrocatalyst is 739.8 mA mg$_{Pt}$$^{-1}$, which is 2.19 times and 4.36 times higher than the Pt/C (337.6 mA mg^{-1}$_{Pt}$) and Pt-rGO (169.7 mA mg^{-1}$_{Pt}$) electrocatalyst, respectively. The magnified CV curves (inset in Figure 4a) shows that Pt-SnO$_2$−prGO also exhibits the lowest onset oxidation potential, because it is relative to the activation energy for the catalyst to trigger MOR.[34] Furthermore, the accelerated stability of as-synthesized electrocatalyst toward MOR was evaluated by the continued CV cycles.[35] Figure 4b presents the normalized forward peak current densities with the number of CV cycles, whereas Figure S6a−c shows the CV curves before and after 1000 cycles. It is particularly informative that Pt-SnO$_2$−prGO only had a moderate loss of about 24% of its initial activity after 1000 cycles, which is 2.08 and 3.21 times better than that of Pt/C (50% loss) and Pt-rGO catalysts (77% loss), respectively. Thus, it is clearly demonstrated that the Pt-SnO$_2$−prGO hybrid exhibits remarkably high electrocatalytic activity and durability toward MOR in contrast to the Pt-rGO and Pt/C.

The electrocatalytic activities and durability were further revalidated by the long-time chronoamperometry (CA). In Figure 5a, current decay is observed for all as-prepared catalysts,
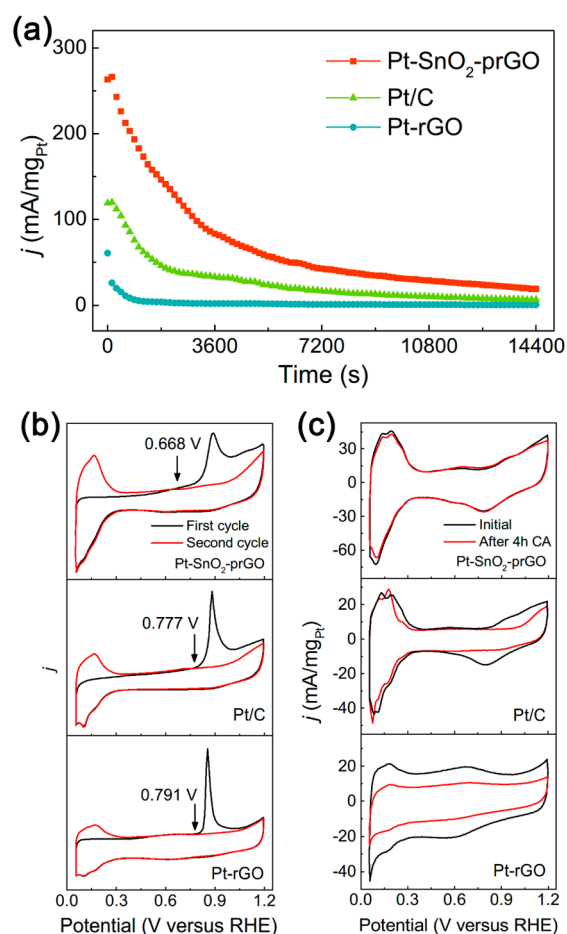

Figure 5. CA plots at 0.8 V (a) on Pt-SnO$_2$−prGO, Pt/C, and Pt-rGO in 2 M CH$_3$OH + 0.1 M H$_2$SO$_4$ solution. CO stripping voltammetry (b) of Pt-SnO$_2$−prGO, Pt/C and Pt-rGO in N$_2$-saturated 0.5 M H$_2$SO$_4$ solution. CV curves (c) of Pt-SnO$_2$−prGO, Pt/C and Pt-rGO in N$_2$-saturated 0.5 M H$_2$SO$_4$ solution before and after 4 h of CA.

ascribed to the formation of some intermediated species (CO$_{ads}$ and CHO$_{ads}$) during the methanol oxidation[27] and the consumption of methanol. During the 4 h period of measurement, the Pt-SnO$_2$−prGO exhibited the highest current density with the lowest deterioration rate among as-prepared catalysts, which is in good agreement with the above CV results. Compared to Pt/C and Pt-rGO, the retainable and high output current of Pt-SnO$_2$−prGO can be ascribed to effectively eliminate the intermediate species adsorbed on the Pt, which made the active site re-exposed.[36,37] The intermediate species oxidation enhanced by SnO$_2$−prGO was confirmed by CO stripping measurements in 0.5 M H$_2$SO$_4$ (Figure 5b). The onset potential for Pt-SnO$_2$−prGO (0.668 V) was lower than that of either Pt/C (0.777 V) or Pt-rGO (0.791 V), demonstrating that the Pt-SnO$_2$−prGO catalyst can oxidize the CO$_{ads}$ species more efficiently than other catalysts at the lower potential. According to the above structural characterization, the electronic effect and cocatalytic functionality should be taken into account. First, the SMSI may change the electronic structure of Pt and thus weaken its binding energy of poisoning intermediates.[10,31] Second, hydroxyls terminated at the surface of SnO$_2$ NPs in SnO$_2$−prGO might oxidize intermediate species absorbed at adjacent Pt sites. However, the more detailed mechanism of this promotion still need to be further investigated.

To clarify the high durability of Pt-SnO$_2$−prGO electrocatalyst, CVs in 0.5 M N$_2$-saturated H$_2$SO$_4$ solution were performed before and after the measurement of a 4 h CA test (Figure 5c). The electrochemical surface areas (ECSA) of as-prepared catalysts were calculated from these CV curves, and the results were listed in Table. S1. Pt/C suffered 15% loss in ECSA and disappearance of Pt oxide formation/reduction peaks, which may be the result of the Ostwald ripening and aggregation of Pt as well as the corrosion of the carbon support.[38] It needs to be pointed out that the electrochemical corrosion of carbon during the operation has been recognized as another main obstacle precluding their application of electrocatalyst.[7,38] For the Pt-rGO, the hydrogen absorption/desorption region becomes less obvious, and the double-layer capacitance of rGO is lost significantly, suggesting the severe corrosion on both Pt NPs and rGO sheets. As measured above, the Pt-rGO catalyst is poorer in both activity and durability than Pt/C, which might be ascribed to the separation of Pt from the electrolyte by the restack of rGO and the corrosion of the exposed defect cluster on rGO where the Pt NPs were loaded. However, the CV curves of Pt-SnO$_2$−prGO showed insignificant change (6% loss in ECSA) in the whole range. In addition, Figure S7 was the TEM image of Pt-SnO$_2$−prGO after a 4 h CA measurement, demonstrating no prominent change for the size or distribution of Pt NPs. Therefore, the SnO$_2$−prGO possesses a robust structure where the defect clusters of rGO are protected by SnO$_2$ NPs, thus the corrosion of the support is inhibited in Pt-SnO$_2$−prGO. The moderate loss in ECSA can be attributed to the stabilization of Pt NPs by ultrafine SnO$_2$ NPs, and hence Ostwald ripening and aggregation of Pt can be largely avoided.

4. CONCLUSION

In summary, the SnO$_2$−prGO nanostructured hybrid was synthesized via an in situ and synergetic strategy, and ultrafine Pt NPs were loaded on this hybrid material. In the obtained Pt-SnO$_2$−prGO nanostructured electrocatalyst, the rGO sheet can uniformly disperse ultrafine SnO$_2$ NPs and provide the network of electron conductivity, whereas the resulting SnO$_2$ NPs can protect the defect cluster remained on rGO, stabilize and afford interaction with Pt NPs. Hence, the significant enhancement of electrocatalytic performance by the strong metal−support interaction, cocatalytic functionality, anticorrosion as well as high surface area and electrical conductivity is achieved. Electrochemical analyses show this strongly coupled Pt-SnO$_2$−prGO electrocatalyst exhibits unexpected, surprisingly high MOR activities and durability, far exceeding that of Pt-rGO and Pt/C. We also demonstrate that the origin of improved performance is attributed to not only the intrinsic properties of metal oxide and graphene but also the synergetic effect within the whole Pt-SnO$_2$−prGO electrocatalyst. This work might provide some clues that the utility of strongly coupled electrocatalyst could open up a brand new approach to advanced catalyst for energy conversion.

◼ ASSOCIATED CONTENT

ⓢ Supporting Information

TEM image, Digital images, Pt 4f XPS spectra, CV curves, and table of ECSA result. This material is available free of charge via the Internet at http://pubs.acs.org.

◼ AUTHOR INFORMATION

Corresponding Author

*E-mail: liuyingju@hotmail.com. Fax: 86-020-85282366. Tel.: 86-020-85280325.

Notes

The authors declare no competing financial interest.

◼ ACKNOWLEDGMENTS

◼ REFERENCES

(1) Kowal, A.; Li, M.; Shao, M.; Sasaki, K.; Vukmirovic, M. B.; Zhang, J.; Marinkovic, N. S.; Liu, P.; Frenkel, A. I.; Adzic, R. R. Ternary Pt/Rh/SnO$_2$ Electrocatalysts for Oxidizing Ethanol to CO$_2$. Nat. Mater. 2009, 8, 325−330.

(2) Bell, A. T. The Impact of Nanoscience on Heterogeneous Catalysis. Science 2003, 299, 1688−1691.

(3) Cargnello, M.; Doan-Nguyen, V. V. T.; Gordon, T. R.; Diaz, R. E.; Stach, E. A.; Gorte, R. J.; Fornasiero, P.; Murray, C. B. Control of Metal Nanocrystal Size Reveals Metal−Support Interface Role for Ceria Catalysts. Science 2013, 341, 771−773.

(4) Shi, J. On the Synergetic Catalytic Effect in Heterogeneous Nanocomposite Catalysts. Chem. Rev. 2013, 113, 2139−2181.

(5) Vayssilov, G. N.; Lykhach, Y.; Migani, A.; Staudt, T.; Petrova, G. P.; Tsud, N.; Skála, T.; Bruix, A.; Illas, F.; Prince, K. C.; Matolín, V. r.; Neyman, K. M.; Libuda, J. Support Nanostructure Boosts Oxygen Transfer to Catalytically Active Platinum Nanoparticles. Nat. Mater. 2011, 10, 310−315.

(6) Kou, R.; Shao, Y.; Mei, D.; Nie, Z.; Wang, D.; Wang, C.; Viswanathan, V. V.; Park, S.; Aksay, I. A.; Lin, Y.; Wang, Y.; Liu, J. Stabilization of Electrocatalytic Metal Nanoparticles at Metal−Metal Oxide−Graphene Triple Junction Points. J. Am. Chem. Soc. 2011, 133, 2541−2547.

(7) Thanh Ho, V. T.; Pillai, K. C.; Chou, H. L.; Pan, C. J.; Rick, J.; Su, W. N.; Hwang, B. J.; Lee, J. F.; Sheu, H. S.; Chuang, W. T. Robust Non-Carbon Ti$_{0.7}$Ru$_{0.3}$O$_2$ Support with Co-Catalytic Functionality for Pt: Enhances Catalytic Activity and Durability for Fuel Cells. Energy Environ. Sci. 2011, 4, 4194−4200.

(8) Liu, Y.; Mustain, W. E. High Stability, High Activity Pt/ITO Oxygen Reduction Electrocatalysts. J. Am. Chem. Soc. 2013, 135, 530−533.

(9) Ta, N.; Liu, J.; Chenna, S.; Crozier, P. A.; Li, Y.; Chen, A.; Shen, W. Stabilized Gold Nanoparticles on Ceria Nanorods by Strong Interfacial Anchoring. J. Am. Chem. Soc. 2012, 134, 20585−20588.

(10) Campbell, C. T. Catalyst−Support Interactions: Electronic Perturbations. Nat. Chem. 2012, 4, 597−598.

(11) Liang, Y.; Li, Y.; Wang, H.; Dai, H. Strongly Coupled Inorganic/Nanocarbon Hybrid Materials for Advanced Electrocatalysis. J. Am. Chem. Soc. 2013, 135, 2013−2036.

(12) Murata, N.; Suzuki, T.; Kobayashi, M.; Togoh, F.; Asakura, K. Characterization of Pt-Doped SnO$_2$ Catalyst for a High-Performance Micro Gas Sensor. Phys. Chem. Chem. Phys. 2013, 15, 17938−17946.

(13) Tripkovic, V.; Cerri, I.; Nagami, T.; Bligaard, T.; Rossmeisl, J. Platinum Redispersion on Metal Oxides in Low Temperature Fuel Cells. Phys. Chem. Chem. Phys. 2013, 15, 3279−3285.

(14) Sun, S.; Zhang, G.; Gauquelin, N.; Chen, N.; Zhou, J.; Yang, S.; Chen, W.; Meng, X.; Geng, D.; Banis, M. N.; Li, R.; Ye, S.; Knights, S.; Botton, G. A.; Sham, T. K.; Sun, X. Single-Atom Catalysis Using Pt/

10263

dx.doi.org/10.1021/am5016606 | ACS Appl. Mater. Interfaces 2014, 6, 10258−10264

Graphene Achieved through Atomic Layer Deposition. *Sci. Rep.* **2013**, 3, 1775.

(15) Liang, J.; Wei, W.; Zhong, D.; Yang, Q.; Li, L.; Guo, L. One-Step In Situ Synthesis of SnO_2/Graphene Nanocomposites and Its Application as an Anode Material for Li-ion Batteries. *ACS Appl. Mater. Interfaces* **2012**, 4, 454−459.

(16) Yang, S.; Yue, W.; Zhu, J.; Ren, Y.; Yang, X. Graphene-Based Mesoporous SnO_2 with Enhanced Electrochemical Performance for Lithium-Ion Batteries. *Adv. Funct. Mater.* **2013**, 23, 3570−3576.

(17) Wang, Y. X.; Lim, Y. G.; Park, M. S.; Chou, S. L.; Kim, J. H.; Liu, H. K.; Dou, S. X.; Kim, Y. J. Ultrafine SnO_2 Nanoparticle Loading onto Reduced Graphene Oxide as Anodes for Sodium-Ion Batteries with Superior Rate and Cycling Performances. *J. Mater. Chem. A* **2014**, 2, 529−534.

(18) Wu, B.; Zheng, N. Surface and Interface Control of Noble Metal Nanocrystals for Catalytic and Electrocatalytic Applications. *Nano Today* **2013**, 8, 168−197.

(19) Kumar, P. V.; Bardhan, N. M.; Tongay, S.; Wu, J.; Belcher, A. M.; Grossman, J. C. Scalable Enhancement of Graphene Oxide Properties by Thermally Driven Phase Transformation. *Nat. Chem.* **2014**, 6, 151−158.

(20) Marcano, D. C.; Kosynkin, D. V.; Berlin, J. M.; Sinitskii, A.; Sun, Z.; Slesarev, A.; Alemany, L. B.; Lu, W.; Tour, J. M. Improved Synthesis of Graphene Oxide. *ACS Nano* **2010**, 4, 4806−4814.

(21) Mason, C. W.; Kannan, A. M. Study of Carbon Nanotube-Supported Platinum Nanocatalyst Fabricated with Sodium Formate Reducing Agent in Ethylene Glycol Suspension. *ISRN Nanotechnol.* **2011**, 2011, 1−6.

(22) Meng, H.; Xie, F.; Chen, J.; Sun, S.; Shen, P. K. Morphology Controllable Growth of Pt Nanoparticles/Nanowires on Carbon Powders and Its Application as Novel Electro-Catalyst for Methanol Oxidation. *Nanoscale* **2011**, 3, 5041−5048.

(23) Yang, S.; Zhao, C.; Ge, C.; Dong, X.; Liu, X.; Liu, Y.; Fang, Y.; Wang, H.; Li, Z. Ternary Pt−Ru−SnO_2 Hybrid Architectures: Unique Carbon-Mediated 1-D Configuration and Their Electrocatalytic Activity to Methanol Oxidation. *J. Mater. Chem.* **2012**, 22, 7104−7107.

(24) Song, H.; Zhang, L.; He, C.; Qu, Y.; Tian, Y.; Lv, Y. Graphene Sheets Decorated with SnO_2 Nanoparticles: In Situ Synthesis and Highly Efficient Materials for Cataluminescence Gas Sensors. *J. Mater. Chem.* **2011**, 21, 5972−5977.

(25) Xu, Y.; Sheng, K.; Li, C.; Shi, G. Highly Conductive Chemically Converted Graphene Prepared from Mildly Oxidized Graphene Oxide. *J. Mater. Chem.* **2011**, 21, 7376−7380.

(26) Gubbala, S.; Russell, H. B.; Shah, H.; Deb, B.; Jasinski, J.; Rypkema, H.; Sunkara, M. K. Surface Properties of SnO_2 Nanowires for Enhanced Performance with Dye-Sensitized Solar Cells. *Energy Environ. Sci.* **2009**, 2, 1302−1309.

(27) Huang, Y.; Huang, H.; Liu, Y.; Xie, Y.; Liang, Z.; Liu, C. Facile Synthesis of Poly(amidoamine)-modified Carbon Nanospheres Supported Pt Nanoparticles for Direct Methanol Fuel Cells. *J. Power Sources* **2012**, 201, 81−87.

(28) Kim, J.; Cote, L. J.; Huang, J. Two Dimensional Soft Material: New Faces of Graphene Oxide. *Acc. Chem. Res.* **2012**, 45, 1356−1364.

(29) Zhang, Q.; Zheng, H.; Geng, Z.; Jiang, S.; Ge, J.; Fan, K.; Duan, S.; Chen, Y.; Wang, X.; Luo, Y. The Realistic Domain Structure of As-synthesized Graphene Oxide from Ultrafast Spectroscopy. *J. Am. Chem. Soc.* **2013**, 135, 12468−12474.

(30) Singh, J. A.; Overbury, S. H.; Dudney, N. J.; Li, M. J.; Veith, G. M. Gold Nanoparticles Supported on Carbon Nitride: Influence of Surface Hydroxyls on Low Temperature Carbon Monoxide Oxidation. *ACS Catal.* **2012**, 2, 1138−1146.

(31) Ganesh, P.; Kent, P. R. C.; Veith, G. M. Role of Hydroxyl Groups on the Stability and Catalytic Activity of Au Clusters on a Rutile Surface. *J. Phys. Chem. Lett.* **2011**, 2, 2918−2924.

(32) Chang, J.; Feng, L.; Liu, C.; Xing, W.; Hu, X. Ni_2P Enhances the Activity and Durability of Pt Anode Catalyst in Direct Methanol Fuel Cells. *Energy Environ. Sci.* **2014**, 7, 1628−1632.

(33) Akalework, N. G.; Pan, C. J.; Su, W. N.; Rick, J.; Tsai, M. C.; Lee, J. F.; Lin, J. M.; Tsai, L. D.; Hwang, B. J. Ultrathin TiO_2-Coated MWCNTs with Excellent Conductivity and SMSI Nature as Pt Catalyst Support for Oxygen Reduction Reaction in PEMFCs. *J. Mater. Chem.* **2012**, 22, 20977−20985.

(34) Chen, T.; Luo, T. J. M.; Yang, Y. W.; Wei, Y. C.; Wang, K. W.; Lin, T. L.; Wen, T. C.; Lee, C. H. Core Dominated Surface Activity of Core−Shell Nanocatalysts on Methanol Electrooxidation. *J. Phys. Chem. C* **2012**, 116, 16969−16978.

(35) Chu, Y. Y.; Wang, Z. B.; Jiang, Z. Z.; Gu, D. M.; Yin, G. P. A Novel Structural Design of a Pt/C-CeO_2 Catalyst with Improved Performance for Methanol Electro-oxidation by Beta-Cyclodextrin Carbonization. *Adv. Mater.* **2011**, 23, 3100−3104.

(36) Zhao, Z.; Yao, Z.; Zhang, J.; Zhu, R.; Jin, Y.; Li, Q. Rational Design of Galvanically Replaced Pt-anchored Electrospun WO_3 Nanofibers as Efficient Electrode Materials for Methanol Oxidation. *J. Mater. Chem.* **2012**, 22, 16514−16519.

(37) Suntivich, J.; Xu, Z.; Carlton, C. E.; Kim, J.; Han, B.; Lee, S. W.; Bonnet, N.; Marzari, N.; Allard, L. F.; Gasteiger, H. A.; Hamad-Schifferli, K.; Shao-Horn, Y. Surface Composition Tuning of Au−Pt Bimetallic Nanoparticles for Enhanced Carbon Monoxide and Methanol Electro-Oxidation. *J. Am. Chem. Soc.* **2013**, 135, 7985−7991.

(38) Sun, S.; Zhang, G.; Geng, D.; Chen, Y.; Li, R.; Cai, M.; Sun, X. A Highly Durable Platinum Nanocatalyst for Proton Exchange Membrane Fuel Cells: Multiarmed Starlike Nanowire Single Crystal. *Angew. Chem., Int. Ed.* **2011**, 50, 422−426.